SCIENTIFIC REPORTS

OPEN

SUBJECT AREAS:
CATALYST SYNTHESIS
ELECTROCATALYSIS

Received
14 November 2013

Accepted
2 January 2014

Published
22 January 2014

Correspondence and requests for materials should be addressed to J.Y. (jyang@mail.ipe.ac.cn)

Selective electrocatalysts toward a prototype of the membraneless direct methanol fuel cell

Yan Feng[1,2], Jinhua Yang[3], Hui Liu[1,2], Feng Ye[1] & Jun Yang[1,3]

[1]State Key Laboratory of Multiphase Complex Systems, Institute of Process Engineering, Chinese Academy of Sciences, Beijing, China 100190, [2]University of Chinese Academy of Sciences, No. 19A Yuquan Road, Beijing, China 100049, [3]Institute of Bioengineering and Nanotechnology, 31 Biopolis Way, The Nanos, 04-01, Singapore 138669.

Mastery over the structure of nanomaterials enables control of their properties to enhance their performance for a given application. Herein we demonstrate the design and fabrication of Pt-based nanomaterials with enhanced catalytic activity and superior selectivity toward the reactions in direct methanol fuel cells (DMFCs) upon the deep understanding of the mechanisms of these electrochemical reactions. In particular, the ternary Au@Ag_2S-Pt nanocomposites display superior methanol oxidation reaction (MOR) selectivity due to the electronic coupling effect among different domains of the nanocomposites, while the cage-bell structured Pt-Ru nanoparticles exhibit excellent methanol tolerance for oxygen reduction reaction (ORR) at the cathode because of the differential diffusion of methanol and oxygen in the porous Ru shell of the cage-bell nanoparticles. The good catalytic selectivity of these Pt-based nanomaterials *via* structural construction enables a DMFC to be built without a proton exchange membrane between the fuel electrode and the oxygen electrode.

The strong growing interest in using direct methanol fuel cells (DMFCs) as portable and mobile power sources is rooted in their desirable features of relatively small environmental footprint, compact system design, and higher volumetric energy densities compared with existing technologies[1,2]. The anode and cathode catalysts of DMFCs are commonly based on Pt[3–8]. These catalysts are not selective to methanol oxidation reaction (MOR) at anode or oxygen reduction reaction (ORR) at cathode, and hence any methanol crossover from the anode to the cathode through the proton exchange membrane can be oxidized by the cathode catalyst. This results in the creation of a mixed potential at the cathode, which degrades the fuel cell performance[9–11]. Although a number of efforts have been devoted toward the modification on the proton exchange membrane to overcome this key obstacle for the commercialization of DMFCs, it is generally thought that the commonly used Nafion membrane has an unacceptably high rate of methanol crossover[12–18]. In this sense, synthesis of electrocatalysts with high selectivity for MOR and ORR represents an alternative for solving this problem in DMFCs.

This work aims at the exploration of Pt-based selective electrocatalysts for DMFCs. Upon the deep understanding of the mechanisms of the electrocatalytic reactions, the Pt-based nanomaterials with enhanced catalytic activity and high selectivity towards DMFC reactions are designed and fabricated for sufficiently making use of the structural uniqueness and electronic coupling effects among the different domains of the electrocatalysts so that the DMFCs can be operated well without or with little dependence on the proton exchange membrane. Herein, we focuses on the controllable syntheses, characterizations, and electrochemical measurements of the Pt-based nanomaterials and the evaluation of their performance as selective catalysts in a prototype of membraneless DMFC. The investigations of the intrinsic relationship between the catalytic properties and the physical or/and chemical effects in the Pt-based nanomaterials might provide for theoretical and technical bases for effectively developing novel electrocatalysts with low cost, enhanced activity, and high selectivity.

Results and discussion

TernaryAu@Ag_2S-Pt nanocomposites as selective electrocatalysts at DMFC anode. Platinum (Pt) nanoparticles are catalytically active for both the anodic and cathodic reactions of the DMFCs[2–4]. However, at room and moderate temperatures, they could be readily poisoned by carbon monoxide (CO), an intermediate product of methanol oxidation[2–7,9–11]. The design of electrocatalysts for improved activity, selectivity and resistance to deactivation should be rational and based on a sufficiently good understanding of the reaction

mechanism. The nature of the Pt–CO bond in MOR has been well documented[19]. The chemisorption of CO on Pt involves the donation of an electron pair from the CO σ* anti-bonding orbitals to the empty 5d-orbitals of Pt. The back donation of electrons from Pt to the CO orbitals further stabilizes their interaction. Thus, the dative electron donation from CO to Pt is a prerequisite for strong CO chemisorption. With this understanding, Ag_2S-Au-Pt composite nanocatalysts have been developed to ameliorate the CO deactivation[20]. The electron transfer from Au and Ag_2S to Pt in Ag_2S-Au-Pt nanocomposites due to the alignment of energy levels (Fig. 1a) increases the electron density around the Pt sites, causing the weakening of CO chemisorption and hence the increase in MOR activity. In contrast, for the Ag_2S-Au-Pt nanocomposites, the electron donation from the semiconductor to the Pt domains would decrease the 5 d vacancies in Pt. Thus, the adsorption of O_2 on the nanocomposites would be too weak for the O_2 dissociation reaction. This would result in poor activity of the Ag_2S-Au-Pt nanocomposites towards ORR, and render the Ag_2S-Au-Pt nanocomposites a good selective catalyst for MOR at the DMFC anode electrode.

Different from that in our previous report[20], in the design of this work, Au was placed at the core region of the nanocomposites for the sufficient utilization of the surface of Ag_2S nanocrystals, as shown in Fig. 1b. The TEM and HRTEM images of the Au seeds and core-shell Au@Ag_2S intermediates for the formation of Au@Ag_2S-Pt nanocomposites were presented in Fig. S1 of Supplementary Information (SI). The Au seed particles were spherical, nearly monodispersed, and had an average size of ~5 nm (SI Fig. S1a). The HRTEM image (SI Fig. S1b) illustrated the lattice planes in these seeds, showing an interplanar spacing of ~0.24 nm, which corresponded to the {111} planes of face-centered cubic (fcc) Au (JCPDS 893697). After coating with Ag_2S shell, the average size of the core-shell nanoparticles was increased to ~9.6 nm, suggesting an Ag_2S shell with average thickness of ~2.4 nm was formed on the surface of each Au seed particle. The core and shell regions of the core-shell Au@Ag_2S nanoparticles could be easily differentiated by the brightness contrast, as shown by the TEM and STEM images in SI Fig. S1c and 1e, respectively, which were significantly different from that of the Au seed particles before the Ag_2S coating (SI Fig. S1a). Additional structural details are revealed by the HRTEM image (SI Fig. S1d), which indicated that the crystal planes of the Au cores were not parallel to those of the Ag_2S shell in core-shell Au@Ag_2S nanoparticles. EDX analysis (SI Fig. S1f) of an arbitrary nanoparticle under STEM mode (as boxed in SI Fig. S1e) further illustrated that the core-shell particle was composed of Ag_2S and Au.

The reduction of K_2PtCl_4 by sodium citrate in the presence of core-shell Au@Ag_2S nanoparticles would result in the formation of ternary Au@Ag_2S-Pt nanocomposites. The reaction temperature was controlled at 110°C. Analogous to the results reported previously[20], Pt nucleated preferentially on the surface of existing Ag_2S shells rather than homogeneously under the experimental conditions. The ternary Au@Ag_2S-Pt nanocomposites obtained were illustrated in Fig. 2. The superposition of the interference patterns of Au, Ag_2S, and Pt made it difficult to differentiate among these domains in the HRTEM images (Fig. 2b). However, the deposition of Pt on the Ag_2S shells could be clearly identified by the brightness contrasts in TEM and STEM images (Fig. 2a and c). By comparison to the TEM and STEM images in SI Fig. S1 (SI Fig. S1c and 1e), the domains with enhanced contrast and larger particle size (~5 nm) in the nanocomposites could be indexed to gold, whereas the Pt metal in the same nanocomposites appeared as smaller dots (~1 nm). The presence of Au, Pt, and Ag_2S in the nanocomposites was confirmed by the EDX analysis (Fig. 2d) performed on an arbitrary particle under the STEM mode (as boxed in Fig. 2c).

The ternary Au@Ag_2S-Pt nanocomposites were examined for their catalytic activities towards the room-temperature methanol oxidation reaction (MOR) and oxygen reduction reaction (ORR), and benchmarked against those of the commercial Pt/C catalysts (E-TEK, 20 wt% Pt nanoparticles (3.2 nm) on Vulcan XC-72 carbon support). As expected, the ternary Au@Ag_2S-Pt nanocomposites displayed superior catalytic activity toward room-temperature methanol oxidation reaction (MOR). The voltammograms of methanol oxidation were obtained in the potential window of 0–1 V at a sweeping rate of 20 mV s^{-1} (Fig. 2e). The peak current densities associated with methanol oxidation in the forward and reverse scans were summarized in SI Table S1. The comparison in current densities indicated that the ternary Au@Ag_2S-Pt nanocomposites showed higher catalytic activity than that of the commercial Pt/C nanoparticles due to the electronic coupling between Pt and the other domains in the nanocomposites. The long-term performance of ternary Au@Ag_2S-Pt nanocomposites and commercial Pt/C catalysts in methanol oxidation was illustrated in the chronoamperograms in SI Fig. S2, in which the slower rate of decay for the Au@Ag_2S-Pt nanocomposites indicated their superior stability to the commercial Pt/C catalysts.

However, contrary to their high catalytic activity for MOR, the ternary Au@Ag_2S-Pt nanocomposites exhibited quite poor activity for ORR. The polarization curves for the ORR over ternary Au@Ag_2S-Pt nanocomposites and commercial Pt/C catalysts were presented in Fig. 2f. SI Table S2 summarized the ORR catalytic activities of these materials at room temperature. The half-wave potential for the ternary Au@Ag_2S-Pt nanocomposites was 479 mV, only 77.4% of commercial Pt/C catalysts (619 mV). The kinetic current density at half-wave potential of the nanocomposites was also much lower than that of commercial Pt/C catalysts. The high MOR activity but poor ORR activity due to the electronic coupling render the ternary Au@Ag_2S-Pt nanocomposites a good candidate as a selective catalyst for MOR at anode of DMFC.

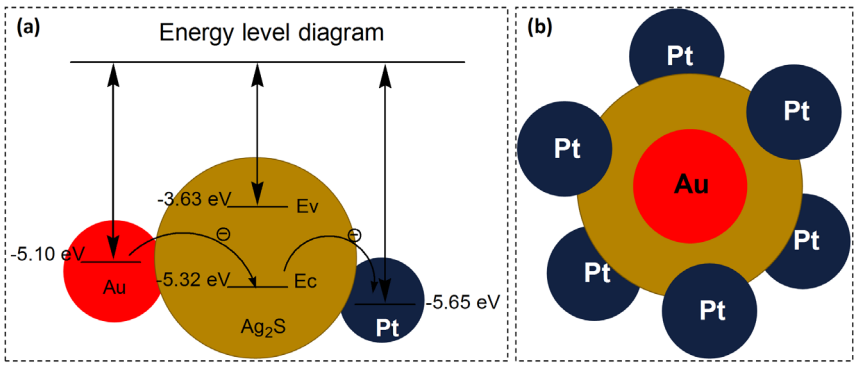

Figure 1 | Schemes. Schematic illustration of the energy level alignment in Ag_2S-Au-Pt nanocomposites (a) and the construction of ternary Au@Ag_2S-Pt nanocomposites (b).

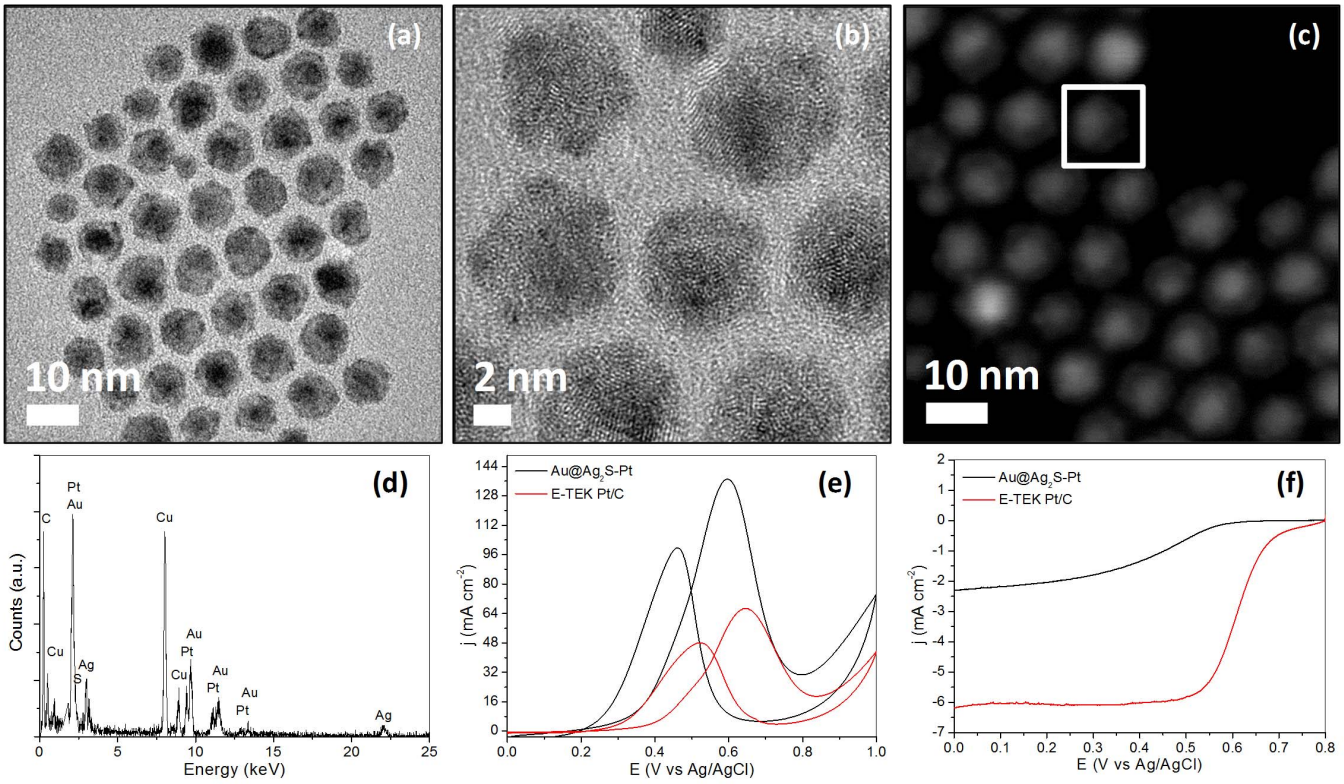

Figure 2 | Ternary Au@Ag_2S-Pt nanocomposites. TEM image (a), HRTEM image (b), STEM image (c), EDX analysis of Au@Ag_2S-Pt nanocomposites (d), cyclic voltammograms of Au@Ag_2S-Pt nanocomposites and commercial Pt/C in argon-purged $HClO_4$ (0.1 M) with methanol of 1 M and sweeping rate of 20 $mV \cdot s^{-1}$ (e), and ORR polarization curves for the Au@Ag_2S-Pt nanocomposites and commercial Pt/C catalysts, recorded at room temperature in an O_2-saturated $HClO_4$ solution (0.1 M) at a sweeping rate of 20 $mV \cdot s^{-1}$ and a rotating speed of 1600 rpm (f).

CBS Pt-Ru nanoparticles as selective electrocatalysts at DMFC cathode. Other than the classical approaches of increasing the Pt catalytic performance through alloying with transition metals[21–24], the good selectivity toward ORR at DMFC cathode could be created by a structural design, rather than the intrinsic properties of the catalytic metals. In this strategy, the bimetallic Pt-Ru nanoparticles with a cage-bell structure were prepared to achieve the ORR selectivity. In the CBS Pt-Ru nanoparticles, the catalytically active metal, i.e. Pt, was located in the core region shielded by a porous Ru shell, which is inactive for methanol oxidation. Reactants must diffuse through the porous shell of the CBS nanoparticles to access the active core for catalytic reaction to occur. In this case the selectivity for ORR might be caused by the porous shell permitting only the passage of small molecule reactants. The situation is depicted by the scheme in Fig. 3. Methanol and oxygen must diffuse into the CBS interior of the nanoparticle through the porous Ru shell for MOR and ORR to occur. However, a methanol molecule is larger than an oxygen molecule (the diameters of methanol and oxygen molecules are 0.44 nm and 0.34 nm, respectively). Hence the diffusion of O_2 is faster than the that of methanol in CBS Pt-Ru nanoparticles, rendering the oxidation of methanol on CBS Pt-Ru a non-competitive event.

The synthesis of CBS Pt-Ru nanoparticles via the core-shell-shell Pt@Ag@Ru nanostructures, where the inner Ag shell serves as the sacrificial component, has been described in our previous report[25]. In this work, the K_2PtCl_4 and $RuCl_3$ metal precursors were replaced with $Pt(acac)_2$ and $Ru(acac)_3$ respectively for the high yield output of the final CBS product. The TEM and HRTEM images of the Pt seeds were shown in SI Fig. S3a and b, respectively. The Pt seed particles were quasi-spherical and had the average size of ~4 nm. After coating with Ag, the size of the nanoparticle was increased to 8.2 nm, and the core-shell structure could be easily differentiated by the brightness contrast in each particle (SI Fig. S3c and d). The subsequent reduction of $Ru(acac)_3$ in the presence of core-shell Pt@Ag nanoparticles resulted in the formation of core-shell-shell Pt@Ag@Ru nanoparticles with average size of ~10.6 nm, as indicated by the TEM, HRTEM, and STEM images in SI Fig. S3e, f, and g, respectively. The core-shell-shell structure could be confirmed by the elemental distributions of an arbitrary single particle, as demonstrated by SI Fig. S3h, which show different distributions for Pt, Ag, and Ru across the particle.

After mixing the core–shell-shell Pt@Ag@Ru nanoparticles with aqueous BSPP solution for 24 h at room temperature, the inner Ag layer was removed from the Pt-Ag-Ru nanoparticles, leaving behind bimetallic Pt-Ru nanoparticles with the cage bell structure in toluene phase. The direct evidence for the Ag removal was provided by the disappearance of Ag signal in the EDX-based line scanning analysis of core-shell-shell Pt@Ag@Ru after the BSPP treatment (Fig. 4d). Electron microscopy images (Fig. 4a, b, and c) showed the preservation of the size and morphology of the core-shell-shell nanoparticles in the CBS nanoparticles. The void space between the Pt core and the outer Ru shell regions, formed upon the elimination of the Ag inner shell by BSPP, is discernible by the strong brightness contrast in TEM, HRTEM, and STEM images. The interplanar spacings of approximate 0.23 nm and 0.21 nm indicated in the HRTEM images of a single CBS Pt-Ru nanoparticle (Fig. 4b) correspond to the (111) plane of face-centered cubic (fcc) Pt and (101) plane of hexagonal Ru, respectively.

Fig. 4e showed the ORR polarization curves in the potential range of 0.8 to 0 V for CBS Pt-Ru nanoparticles and commercial Pt/C catalysts in oxygen-saturated 0.1 M $HClO_4$ at room temperature. The CBS Pt-Ru nanoparticles displayed comparable activity with that of commercial Pt/C catalysts for ORR due to similar particle size, suggesting the porous Ru shell has negligible effect on the

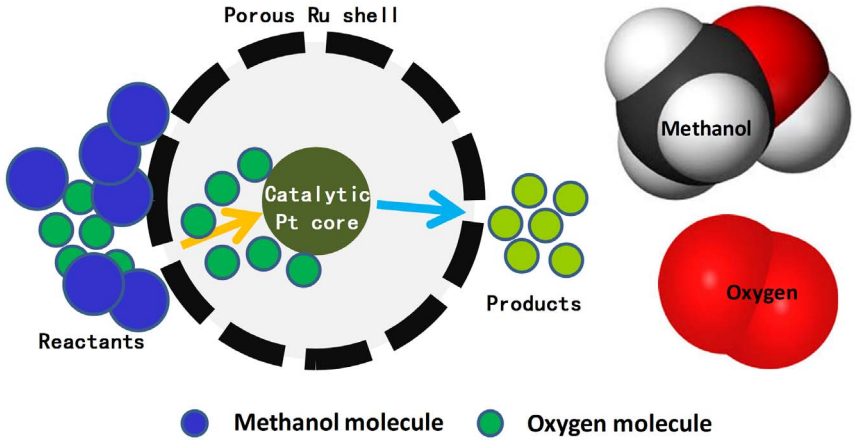

Figure 3 | ORR selectivity by CBS Pt-Ru nanoparticles. Schematic illustration of the differential diffusion and reaction of methanol and oxygen in CBS Pt-Ru nanoparticles.

activity of Pt core for ORR. More importantly, as expected from the structural design, even with the presence of methanol in concentration as high as 1.0 M in the electrolyte, the catalytic reduction of oxygen on the CBS Pt-Ru nanoparticles was hardly affected, demonstrating the effective inhibition of methanol oxidation on the CBS Pt-Ru nanoparticles (Fig. 4e). Correspondingly, as manifested by Fig. 4f, the activity for methanol oxidation over CBS Pt-Ru was almost no detectable in comparison with that of commercial Pt/C catalysts, suggesting CBS Pt-Ru nanoparticles have poor catalytic activity for MOR. By tailoring the structures (e.g. the size of Pt core and the porosity of Ru shell) of the CBS nanoparticles, one would expect the ORR catalytic activity and methanol-tolerant property of CBS Pt-Ru nanoparticles could be further enhanced.

A prototype of the membraneless direct methanol fuel cell. The poor ORR activity of ternary Au@Ag_2S-Pt nanocomposites and methanol-tolerant property of CBS Pt-Ru nanoparticles provided a promising opportunity to construct a membraneless DMFC based solely on the selectivity of the catalysts. The membraneless DMFC shown in Fig. 5a consists of a single compartment vessel with two electrodes in a common electrolyte of 1 M methanol in 0.1 M $HClO_4$. The electrolyte is saturated with dissolved oxygen by

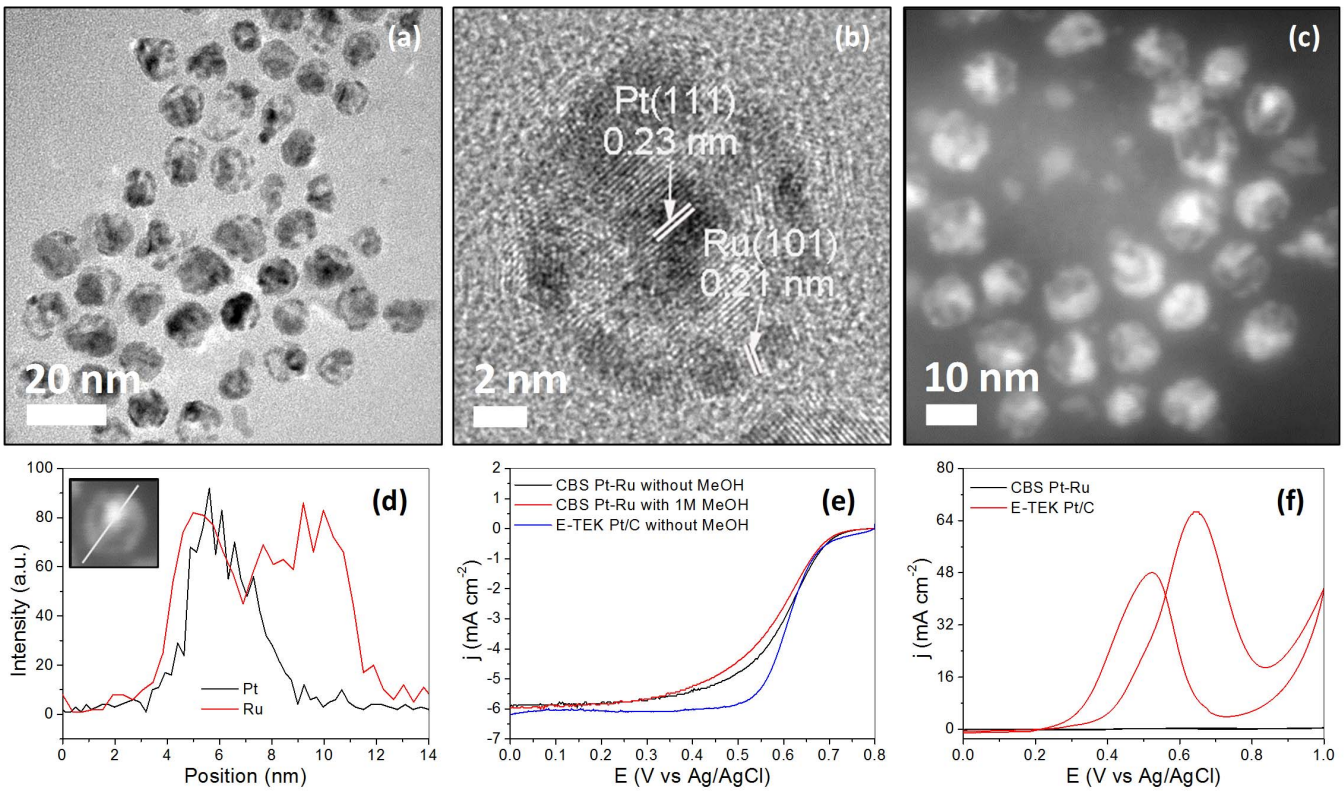

Figure 4 | CBS Pt-Ru nanoparticles. TEM image (a), HRTEM image (b), STEM image (c), EDX-based line scanning analysis of a single CBS Pt-Ru nanoparticle (d), ORR polarization curves for the CBS Pt-Ru nanoparticles and commercial Pt/C catalysts, recorded at room temperature in an O_2-saturated $HClO_4$ solution (0.1 M, with or without 1 M methanol) at a sweeping rate of 20 $mV \cdot s^{-1}$ and a rotating speed of 1600 rpm (e), and cyclic voltammograms of CBS Pt-Ru nanoparticles and commercial Pt/C in argon-purged $HClO_4$ (0.1 M) with methanol of 1 M and sweeping rate of 20 $mV \cdot s^{-1}$ (f).

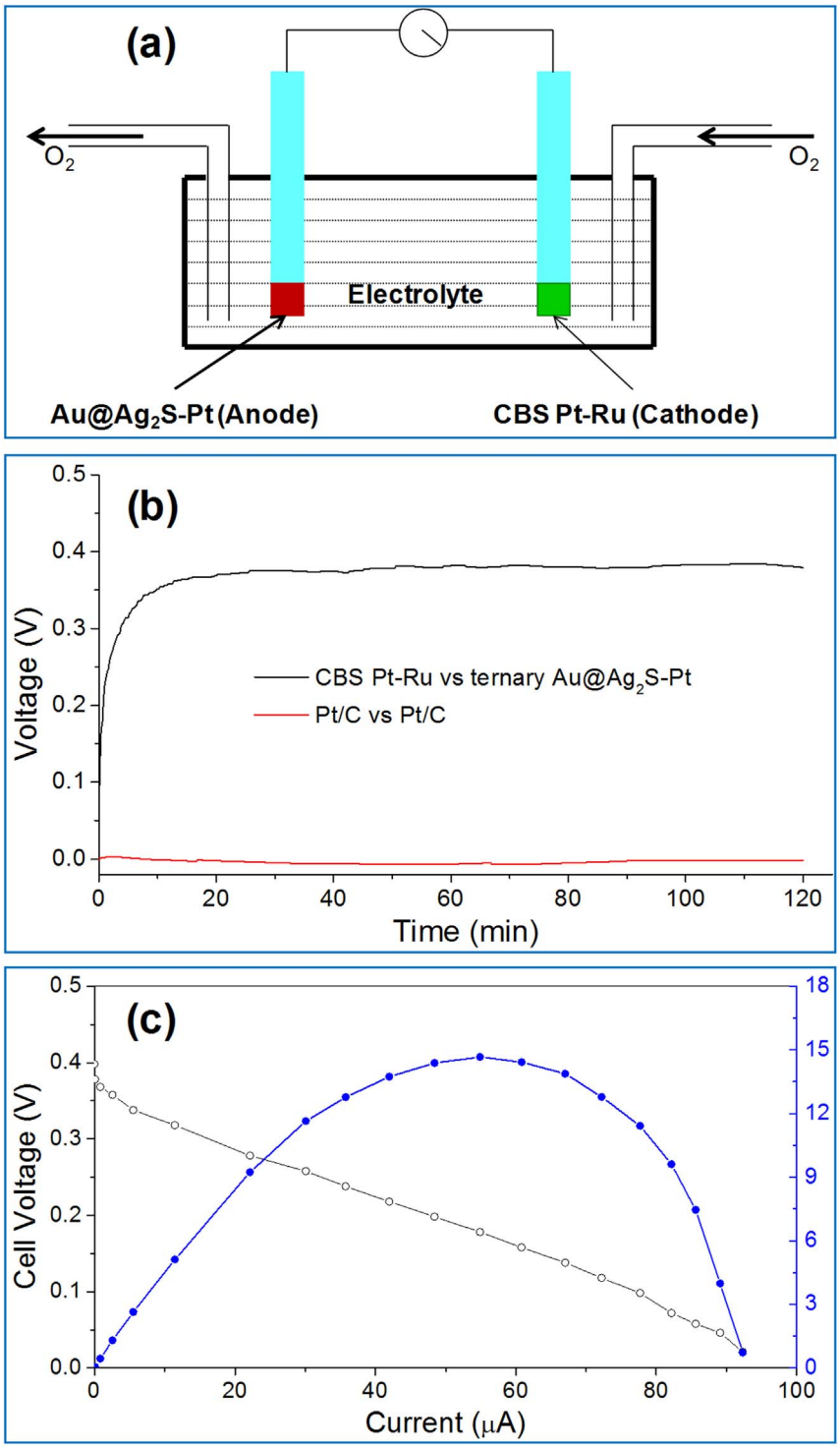

Figure 5 | A prototype of the membraneless DMFC. Schematic for the membraneless DMFC (a), The open-circuit voltage of membraneless DMFC with selective ORR and MOR catalysts in comparison with that of membraneless DMFC using commercial non-selective catalysts (b), and I-V and I-P curves of the membraneless DMFC operated at 1 M methanol under ambient conditions (c).

continuously bubbling O_2 into the solution. The essential prerequisite for a membraneless DMFC is that the anode and cathode catalysts must be highly selective to MOR and ORR respectively. The methanol tolerant CBS Pt-Ru nanoparticles are naturally the cathode ORR-selective catalyst, while the ternary Au@Ag_2S-Pt nanocomposites are served as the MOR-selective catalyst at anode.

The performance of the membraneless DMFC was evaluated in term of the open circuit voltage (OCV), the current-voltage ($I-V$), and the current-power ($I-P$) characteristics under ambient conditions. Fig. 5b shows that the membraneless DMFC with the selective MOR catalyst at the anode and ORR catalyst at the cathode maintained an open-circuit voltage of ~0.38 V for more than 120 min, comparing favourably with the same membraneless fuel cell operating with a non-selective Pt/C catalyst as both anode and cathode catalysts. As shown in Fig. 5c, it is of great importance that reasonable power with the maximum value of ~15 μW was obtained without a separate membrane. The OCV of the membraneless DMFC was still rather low, at only ~32% of the theoretical cell

voltage of DMFC (~1.18 V)[26]. The performance of the prototype could be limited by the use of dissolved oxygen as the source of oxygen. Dissolved oxygen exists only in low concentrations (1–2 mM at room temperature) and has a significantly lower diffusion coefficient (2×10^{-5} cm^2 s^{-1}) than gaseous oxygen (0.2 cm^2 s^{-1})[27,28]. Despite the limited performance, the prototype does demonstrate the viability of using selective MOR and ORR catalysts to construct a DMFC without the proton exchange membrane. Since the exemption of a proton exchange membrane not only reduces the cost and volume of the DMFC, it also provides more flexibility and miniaturizability of the cell design. Its implementation is also simpler than membraneless fuel cells that depend on non-mixing laminar flows[29,30] or 3D anode[31–33]. The performance of the membraneless fuel cell may be improved by using the on-chip fuel cell developed by the Osaka group, which can directly make use of the oxygen from the air[34].

In summary, the ternary Au@Ag_2S-Pt nanocomposites and CBS Pt-Ru nanoparticles were designed and fabricated for sufficiently making use of the structural uniqueness and electronic coupling effects among the different domains of the nanocomposites. In particular, the ternary Au@Ag_2S-Pt nanocomposites displayed superior MOR selectivity, while the CBS Pt-Ru nanoparticles exhibited excellent methanol tolerance for ORR at the cathode of the direct methanol fuel cell. The good catalytic selectivity enabled a DMFC to be built without a proton exchange membrane between the fuel electrode and the oxygen electrode. Through this research effort the researcher may wish to influence a rethinking of the current processing technologies: To move towards molecular-level control and regulation; and away from the "top-down" approach and the stringent and expensive control inherent in conventional manufacturing processes.

Methods

General materials. Ruthenium(III) acetylacetonate ($Ru(acac)_3$, 97%), silver nitrate ($AgNO_3$, 99%), platinum(II) acetylacetonate ($Pt(acac)_2$, 97%), potassium tetrachloroplatinate(II) (K_2PtCl_4, 98%), gold(III) chloride trihydrate ($HAuCl_4 \cdot 3H_2O$, ACS reagent, ≥49.0% Au basis), gold(III) chloride ($AuCl_3$, 99%), oleylamine (70%, technical grade), thioacetamide (C_2H_5NS, ACS reagent, ≥99%), sodium borohydride ($NaBH_4$, 98%), sodium citrate dehydrate ($HOC(COONa)(CH_2COONa)_2 \cdot 2H_2O$, ≥99%), dodecylamine (DDA, 98%), aqueous $HClO_4$ solution (70%, ACS reagent), Methanol (99%), ethanol (99.5%), toluene (99.5%), and Nafion 117 solution (5% in a mixture of lower aliphatic alcohols and water) from Sigma-Aldrich, bis(p-sulfonatophenyl)phenylphosphane dihydrate dipotassium salt (BSPP, 97%) from Strem Chemicals, and Vulcan XC-72 carbon powders (XC-72C, BET surface area = 250 m^2/g and average particle size = 40 ~ 50 nm) from Cabot, were used as received. All glassware and Teflon-coated magnetic stir bars were cleaned with *aqua regia*, followed by copious rinsing with de-ionized water before drying in an oven.

Synthesis of ternary Au@Ag_2S-Pt nanocomposites. The synthesis of ternary Au@Ag_2S-Pt nanocomposites was conducted in aqueous phase. Firstly, citrate-stabilized Au (~5 nm) seed particles were prepared by the $NaBH_4$ reduction of $HAuCl_4$[35]. An aqueous solution of $HAuCl_4$ (1 mM, 100 mL) was mixed with 4 mL of 100 mM aqueous sodium citrate solution used as stabilizer. Then 3 mL of 100 mM aqueous $NaBH_4$ solution was added dropwise under vigorous stirring, giving rise to a wine red hydrosol. The Au hydrosol was then aged for 24 h to decompose the residual $NaBH_4$ before it was used in the next steps.

Subsequently, to the prepared Au hydrosol, 200 mg of BSPP was added, followed by the addition of 2 mL of aqueous $AgNO_3$ solution (50 mM). The mixture was stirred for 30 min at room temperature, and was then heated at 90°C (temperature of the oil bath) in a 250 ml of three-necked flask equipped with a condenser and a Teflon-coated magnetic stirring bar for 3 min. Then 2 mL of 50 mM aqueous thioacetamide solution was added swiftly, and the reaction mixture was continuously heated at 90°C for 120 min to form a hydrosol of core-shell Au@Ag_2S nanoparticles.

For the formation of ternary Au@Ag_2S-Pt nanocomposites, the core-shell Au@Ag_2S hydrosol prepared above was refluxed at 110°C (temperature of the oil bath) for 3 min in a 250 mL three-necked flask equipped with a condenser and a Teflon-coated magnetic stirring bar. Next, 4 mL of aqueous sodium citrate solution (100 mM) was added. The resulting mixture was refluxed for 1 min at 110°C, and then 2 mL of aqueous K_2PtCl_4 solution (50 mM) was added swiftly. The reaction mixture was continuously refluxed at 110°C for 120 min to form a hydrosol of ternary Au@Ag_2S-Pt nanocomposites.

Finally, the as-prepared ternary Au@Ag_2S-Pt nanocomposites were transferred from aqueous phase to toluene using an approach developed for the phase transfer of metal nanoparticles and ions[36,37]. Phase transfer of the nanocomposites from aqueous phase to a non-polar organic medium was conducted since we experimentally found that the loading efficiency of the particles on XC-72C carbon supports from the organic medium (~99%) was much higher than that from the aqueous phase (~37%). Typically, the Au@Ag_2S-Pt hydrosol was mixed with an equal volume of ethanolic solution of DDA (90 mM). After 3 min of stirring, an equal volume of toluene was added and stirred for another minute. Phase transfer of the Au@Ag_2S-Pt nanocomposite from water to toluene would then occur quickly and completely, leaving a clear colorless solution in the aqueous phase. Inductively coupled plasma atomic emission spectroscopy (ICP-AES) analysis showed that the phase transfer efficiency was ~100%.

Synthesis of cage-bell structured Pt-Ru (CBS Pt-Ru) nanoparticles. The synthesis of CBS Pt-Ru nanoparticles followed a reported protocol with slight modification[23]. The Pt seed particles with average size of ~4 nm were prepared first by the oleylamine reduction of $Pt(acac)_2$. Typically, 60 mg of $Pt(acac)_2$ and 5 mg of $AgNO_3$ were added to 20 mL of oleylamine. The small amount of $AgNO_3$ was needed to promote the formation of spherical Pt nanoparticles. The mixture was then heated and kept at 160°C for 1 h with stirring under flowing N_2 to form the Pt seeds. Then 90 mg of $AgNO_3$ was added swiftly and the temperature of the reaction mixture was lowered to 100°C and maintained at this temperature under flowing N_2 for 4 h for the growth of Ag on existing Pt seeds. Subsequently, 70 mg of $RuCl_3$ was added swiftly, followed by heating and keeping the reaction mixture at 320°C for 1 h under flowing N_2 for the reduction of the Ru metal precursor in the presence of previously formed core-shell Pt@Ag nanoparticles. After the reaction, these core-shell-shell Pt@Ag@Ru nanoparticles were purified by precipitation with methanol, centrifugation, washing with methanol, and re-dispersed in 20 mL of toluene.

For the formation of CBS Pt-Ru nanoparticles, the core-shell-shell Pt@Ag@Ru nanoparticle solution was diluted with toluene to 100 mL. An aqueous BSPP solution was prepared by dissolving 2000 mg of BSPP in 100 mL of water. The diluted core-shell-shell Pt@Ag@Ru nanoparticles in toluene and the aqueous BSPP solution were then mixed together. The mixture was aged for 24 h under vigorous stirring at room temperature for the removal of Ag from the inner shell, followed by the collection of the upper toluene phase after complete separation of the two phases.

Particle characterizations. UV-visible spectra of the particle solutions were collected on a Hitachi U-3900 spectrophotometer. Transmission electron microscopy (TEM), high resolution TEM (HRTEM), and scanning TEM (STEM) were performed on the JEOL JEM-2100 and FEI Tecnai G^2 F20 electron microscope operating at 200 kV with a supplied software for automated electron tomography. For the TEM measurements, a drop of the nanoparticle solution was dispensed onto a 3-mm carbon-coated copper grid. Excessive solution was removed by an absorbent paper, and the sample was dried under vacuum at room temperature. An energy dispersive X-ray spectroscopy (EDX) analyzer attached to the TEM operating in the scanning transmission electron microscopy (STEM) mode was used to analyze the chemical compositions of the synthesized nanocomposites or nanoparticles.

Electrochemical measurements. Electrochemical measurements were carried out in a standard three-electrode cell connected to a Bio-logic VMP3 (with EC-lab software version 9.56) potentiostat. A leak-free Ag/AgCl (saturated with KCl) electrode was used as the reference electrode. The counter electrode was a platinum mesh (1×1 cm^2) attached to a platinum wire.

For the loading of the ternary Au@Ag_2S-Pt nanocomposites or CBS Pt-Ru nanoparticles on Vulcan XC-72 carbon support, a calculated amount of carbon powder was added to the toluene solution of ternary Au@Ag_2S-Pt nanocomposites or CBS Pt-Ru nanoparticles. After stirring the mixture for 24 h, the Au@Ag_2S-Pt/C or CBS Pt-Ru/C catalysts (20 wt% Pt on carbon support) was collected by centrifugation, washed thrice with methanol, and then dried at room temperature in vacuum.

The working electrode was a thin layer of Nafion-impregnated catalyst cast on a vitreous carbon disk. This electrode was prepared by ultrasonically dispersing 10 mg of the Au@Ag_2S-Pt/C or CBS Pt-Ru/C catalysts in 10 mL of water containing 4 ml ethanol and 0.1 ml of Nafion solution. A calculated volume of the ink was dispensed onto the 5 mm glassy carbon disk electrode to produce a nominal catalyst loading of 20 μg cm^{-2} (Pt basis). The carbon electrode was then dried in a stream of warm air at 70°C for 1 h.

The performance of ternary Au@Ag_2S-Pt nanocomposites and CBS Pt-Ru nanoparticles in room-temperature methanol oxidation reaction (MOR) was measured by cyclic voltammetry. For these measurements the potential window of 0 V to 1 V was scanned at 20 $mV \cdot s^{-1}$ until a stable response was obtained, before recording the voltammograms. The electrolyte was methanol (1 M) in perchloric acid (0.1 M). and the current densities were all based on the geometric area (0.196 cm^2) of the glassy carbon electrode.

The performance of ternary Au@Ag_2S-Pt nanocomposites and CBS Pt-Ru nanoparticles in room temperature oxygen reduction reaction (ORR) was also evaluated in 0.1 M $HClO_4$ electrolyte solution using a glass carbon rotating disk electrode (RDE) at a rotation rate of 1600 rpm. Negative-going linear sweep voltammograms were recorded from 1 to 0 V at 20 $mV \cdot s^{-1}$ at room temperature in the presence of bubbling ultra-pure oxygen to maintain a saturated oxygen atmosphere near the working electrode. For each catalyst (ternary Au@Ag_2S-Pt nanocomposites or CBS Pt-Ru nanopartickes), the measured current was normalized by the geometric area of the glassy carbon electrode.

1. Antolini, E. Formation of carbon-supported PtM alloys for low temperature fuel cells: a review. *Mater. Chem. Phys.* **78**, 563–573 (2003).

2. Liu, H. *et al.* A review of anode catalysis in the direct methanol fuel cell. *J. Power Sources* **155**, 95–110 (2006).
3. Perry, M. L. & Fuller, T. F. A historical perspective of fuel cell technology in the 20th century. *J. Electrochem. Soc.* **149**, S59–S67 (2002).
4. Steele, B. C. H. & Heinzel, A. Materials for fuel-cell technologies. *Nature* **414**, 345–352 (2004).
5. Wang, X., Waje, M. & Yan, Y. Methanol resistant cathodic catalyst for direct methanol fuel cells. *J. Electrochem. Soc.* **151**, A2183–A2188 (2004).
6. Chen, J., Lim, B., Lee, E. P. & Xia, Y. Shape-controlled synthesis of platinum nanocrystals for catalytic and electrocatalytic applications. *Nano Today* **4**, 81–95 (2009).
7. Peng, Z. & Yang, H. Designer platinum nanoparticles: Control of shape, composition in alloy, nanostructure and electrocatalytic property. *Nano Today* **4**, 143–146 (2009).
8. Xia, B. Y., Wu, H. B., Yan, Y., Low, X. W. & Wang, X. Ultrathin and ultralong single-crystal platinum nanowire assemblies with highly stable electrocatalytic activity. *J. Am. Chem. Soc.* **135**, 9480–9485 (2013).
9. Liu, F., Lu, G. & Wang, C.-Y. Low crossover of methanol and water through thin membranes in direct methanol fuel cells. *J. Electrochem. Soc.* **153**, A543–A553 (2006).
10. Du, C. Y., Zhao, T. S. & Yang, W. W. Effect of methanol crossover on the cathode behavior of a DMFC: A half-cell investigation. *Electrochim. Acta* **52**, 5266–5271 (2007).
11. Antolini, E., Lopes, T. & Gonzalez, E. R. An overview of platinum-based catalysts as methanol-resistant oxygen reduction materials for direct methanol fuel cells. *J. Alloys Compd.* **461**, 253–262 (2008).
12. Jia, N., Lefebvre, M. C., Halfyard, J., Qi, Z. & Pickup, P. G. Modification of Nafion proton exchange membranes to reduce methanol crossover in PEM fuel cells. *Electrochem. Solid-State Lett.* **3**, 529–531 (2000).
13. Gurau, B. & Smotkin, E. S. Methanol crossover in direct methanol fuel cells: a link between power and energy density. *J. Power Sources* **112**, 339–352 (2002).
14. Kim, Y.-M., Park, K.-W., Choi, J.-H., Park, I.-S. & Sung, Y.-E. A Pd-impregnated nanocomposite Nafion membrane for use in high-concentration methanol fuel in DMFC. *Electrochem. Commun.* **5**, 571–574 (2003).
15. Sahu, A. K., Pitchumani, S., Sridhar, P. & Shukla, A. K. Nafion and modified-Nafion membranes for polymer electrolyte fuel cells: An overview. *Bull. Mater. Sci.* **32**, 285–294 (2009).
16. Zhang, H., Huang, H. & Shen, P. K. Methanol-blocking Nafion composite membranes fabricated by layer-by-layer self-assembly for direct methanol fuel cells. *Int. J. Hydrogen Energy* **37**, 6875–6879 (2012).
17. Zhang, Y. *et al.* A modified Nafion membrane with extremely low methanol permeability via surface coating of sulfonated organic silica. *Chem. Commun.* **48**, 2870–2872 (2012).
18. Beauger, C. *et al.* Nafion®-sepiolite composite membranes for improved Proton Exchange Membrane Fuel Cell performance. *J. Membr. Sci.* **130**, 167–179 (2013).
19. Shukla, A. K. *et al.* An X-ray photoelectron spectroscopic study on the effect of Ru and Sn additions to platinised carbons. *Appl. Surf. Sci.* **137**, 20–29 (1999).
20. Yang, J. & Ying, J. Y. Nanocomposites of Ag_2S and noble metals. *Angew. Chem. Int. Ed.* **50**, 4637–4643 (2011).
21. Toda, T., Igarashi, H., Uchida, H. & Watanabe, M. Enhancement of the electroreduction of oxygen on Pt alloys with Fe, Ni, and Co. *J. Electrochem. Soc.* **146**, 3750–3756 (1999).
22. Fernández, J. L., Raghuveer, V., Manthiram, A. & Bard, A. J. Pd−Ti and Pd−Co−Au electrocatalysts as a replacement for platinum for oxygen reduction in proton exchange membrane fuel cells. *J. Am. Chem. Soc.* **127**, 13100–13101 (2005).
23. Yang, J., Lee, J. Y., Zhang, Q., Zhou, W. & Liu, Z. Carbon-supported pseudo-core-shell Pd-Pt nanoparticles for ORR with and without methanol. *J. Electrochem. Soc.* **155**, B776–B781 (2008).
24. Yang, J., Cheng, C. H., Zhou, W., Lee, J. Y. & Liu, Z. Methanol-tolerant heterogeneous PdCo@PdPt/C electrocatalyst for the oxygen reduction reaction. *Fuel Cells* **10**, 907–913 (2010).
25. Liu, H. *et al.* Hollow and cage-bell structured nanomaterials of noble metals. *J. Am. Chem. Soc.* **134**, 11602–11610 (2012).
26. Cameron, D. S., Hards, G. A., Harrison, B. & Potter, R. J. Direct methanol fuel cells. *Platinum Metals Rev.* **31**, 173–181 (1987).
27. Narita, E., Lawson, F. & Han, K. N. Solubility of oxygen in aqueous electrolyte solutions. *Hydrometallurgy* **10**, 21–37 (1983).
28. Jayashree, R. S. *et al.* Air-breathing laminar flow-based microfluidic fuel cell. *J. Am. Chem. Soc.* **127**, 16758–16759 (2005).
29. Ferrigno, R., Stroock, A. D., Clark, T. D., Mayer, M. & Whitesides, G. M. Membraneless vanadium redox fuel cell using laminar flow. *J. Am. Chem. Soc.* **124**, 12930–12931 (2002).
30. Jayashree, R. S. *et al.* Air-breathing laminar flow-based direct methanol fuel cell with alkaline electrolyte. *Electrochem. Solid State Lett.* **9**, A252–A256 (2006).
31. Lam, A., Wilkinson, D. P. & Zhang, J. Novel approach to membraneless direct methanol fuel cells using advanced 3D anodes. *Electrochim. Acta* **53**, 6890–6898 (2008).
32. Lam, A., Wilkinson, D. P. & Zhang, J. Control of variable power conditions for a membraneless direct methanol fuel cell. *J. Power Sources* **194**, 991–996 (2009).
33. Lam, A., Dara, M. S., Wilkinson, D. P. & Fatih, K. Aerobic and anaerobic operation of an active membraneless direct methanol fuel cell. *Electrochem. Commun.* **17**, 22–25 (2012).
34. Tominaka, S., Ohta, S., Obata, H., Momma, T. & Osaka, T. On-chip fuel cell: Micro direct methanol fuel cell of an air-breathing, membraneless, and monolithic design. *J. Am. Chem. Soc.* **130**, 10456–10457 (2008).
35. Qu, J. *et al.* Coalescence of Ag_2S and Au nanocrystals at room temperature. *J. Mater. Chem.* **21**, 11750–11753 (2011).
36. Yang, J., Lee, J. Y., Deivaraj, T. C. & Too, H.-P. A highly efficient phase transfer method for preparing alkylamine-stabilized Ru, Pt, and Au nanoparticles. *J. Colloid Interface Sci.* **277**, 95–99 (2004).
37. Yang, J., Sargent, E. H., Kelley, S. O. & Ying, J. Y. A general phase-transfer protocol for metal ions and its application in nanocrystal synthesis. *Nature Mater.* **8**, 683–689 (2009).

Acknowledgments

Financial support from the 100 Talents Program of the Chinese Academy of Sciences, National Natural Science Foundation of China (No.: 21173226, 21376247), State Key Laboratory of Multiphase Complex Systems, Institute of Process Engineering, Chinese Academy of Sciences (MPCS-2012-A-11, MPCS-2011-D-08, MPCS-2010-C-02), and the Institute of Bioengineering and Nanotechnology (Biomedical Research Council, Agency for Science, Technology and Research, Singapore) is gratefully acknowledged.

Author contributions

F.Y. and H.L. performed the materials synthesis, characterization and electrochemical measurements. J.Y. (Jinhua Yang) and F.Y. contributed to the electrochemical evaluation of the prototype of membraneless DMFC. J.Y. (Jun Yang) supervised the project and wrote the main manuscript text. All authors participated in the review of the manuscript.

Additional information

Supplementary information accompanies this paper at http://www.nature.com/scientificreports

Competing financial interests: The authors declare no competing financial interests.

How to cite this article: Feng, Y., Yang, J., Liu, H., Ye, F. & Yang, J. Selective electrocatalysts toward a prototype of the membraneless direct methanol fuel cell. *Sci. Rep.* **4**, 3813; DOI:10.1038/srep03813 (2014).